Imaging of ballistic carrier transport in tungsten single crystals

A. Böhm, J. Heil, M. Primke, and A. Gröger
Hochfeld-Magnetlabor, Max-Planck-Institut für Festkörperforschung and Centre National de la Recherche Scientifique, Boîte Postale 166, 25 Avenue des Martyrs, F-38042 Grenoble Cedex 9, France

P. Keppler
Max-Planck-Institut für Metallforschung, Institut für Physik, Heisenbergstraße 1, D-70569 Stuttgart, Germany

J. Major
Max-Planck-Institut für Metallforschung, Institut für Physik, Heisenbergstraße 1, D-70569 Stuttgart, Germany and Universität Stuttgart, Institut für Theoretische und Angewandte Physik, Pfaffenwaldring 57, D-70569 Stuttgart, Germany

P. Wyder
Hochfeld-Magnetlabor, Max-Planck-Institut für Festkörperforschung and Centre National de la Recherche Scientifique, Boîte Postale 166, 25 Avenue des Martyrs, F-38042 Grenoble Cedex 9, France

(Received 22 January 1999)

Ballistic carrier transport is studied in real space in tungsten single crystals using carrier excitation by laser light. So-called electron focusing caustics, singularities of the carrier flux in specific directions, have been investigated systematically for crystals in three different orientations. The influence of magnetic fields **B** on the focusing patterns has been studied for different field orientations. Sondheimer oscillations periodic in B have been observed. The experimental data can be described by a simple model based on fully ballistic transport. Calculated focusing patterns are in satisfactory agreement with the experiments. [S0163-1829(99)08527-6]

I. INTRODUCTION

If the mean free path l^* of carriers in metals becomes very large, i.e., in the range of several hundred μm, carriers can pass through samples with thickness d in this range without scattering. This is the so-called ballistic transport regime. To reach these large mean free paths experimentally, special conditions such as low temperatures and very pure and almost perfect crystals are necessary.

This paper presents an application of a technique for the spatially resolved investigation of ballistic carrier transport in the transition metal tungsten. Nonequilibrium carriers are produced thermoelectrically by local heating. This is realized by the illumination of a small area (*hot spot)* on the sample surface by means of a laser and an optical fiber (see Fig. 2).

If scattering is negligible, the transport of nonequilibrium carriers to the opposite sample surface is in general highly anisotropic due to the Fermi surface geometry (i.e., the band structure of the material). The carriers produce a current distribution at the other sample surface. The resulting potential can be detected by a point contact. The fiber can be scanned over the sample surface. This allows real-space-resolved measurements of the current distribution. The detected patterns may be interpreted as a kind of fingerprint of the Fermi surface. Signals produced by electrons and holes can be distinguished by their polarity and by their reaction upon the application of a magnetic field. First results of this method applied to the semimetal bismuth, the noble metal silver, and the transition metal tungsten were published in Refs. 1 and 2. The detected patterns become increasingly complex in this order. This paper reports a systematic investigation of these anisotropic patterns in three differently oriented tungsten single crystals. Furthermore, the influence of a magnetic field applied perpendicular and parallel to the sample slab has been studied.

II. ELECTRON FOCUSING

In the case of ballistic propagation, the carrier transport can be described by the semiclassical model of electronic motion. The group velocity $\mathbf{v}_{gr}$ is given by

$$\mathbf{v}_{gr}=\frac{1}{\hbar}\nabla_k E(\mathbf{k}). \tag{2.1}$$

Here $\hbar=h/(2\pi)$, h is Planck's constant, k is the wave vector, and $\mathbf{v}_{gr}$ is the group-velocity vector. According to Eq. (2.1), $\mathbf{v}_{gr}$ is perpendicular to surfaces of constant energy $\mathsf{S}_{E(\mathbf{k})}$ in $\mathbf{k}$ space: $\mathbf{v}_{gr}\perp\mathsf{S}_E$ [Fig. 1(a)(I)]. Since the excited carriers have an energy distribution very close to the Fermi energy E_F, the consideration of electrons at E_F only is a good approximation to describe how the so-called electron-focusing patterns come about. This is outlined in Fig. 1 for two Fermi surfaces in two-dimensional $\mathbf{k}$ space.

In locations of very small or vanishing curvature of the ''Fermi line'' (i.e., the radius of curvature is infinite) the group-velocity vectors $\mathbf{v}_{gr}$ for neighboring $\mathbf{k}$ states are (almost) parallel. This results in an enhancement of the carrier flux along the associated directions. This is illustrated by the square ''Fermi line'' in Fig. 1(a)(I), and the resulting current distribution in Fig. 1(a)(II).

In Ref. 3 it is shown theoretically that the magnitude of the current density $j(\mathbf{k})$ in three-dimensional space related to

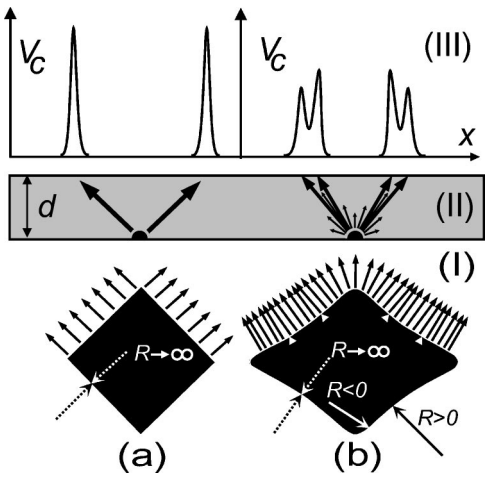

FIG. 1. The coming about of the so-called EF-patterns shown for (a) square and (b) central [110] cross section of the hole octahedron Fermi surface of tungsten. (I) Momentum space; R is the radius of curvature. ▲ indicates the locations with infinite R. The group-velocity vectors ($\mathbf{v}_{gr}$) are perpendicular to the Fermi surfaces and represent the spatial direction of the electronic ballistic current in real space. (II) Real space: the trajectories are straight lines for $B=0$. (III) Signal V_C.

a location on the Fermi surface is proportional to the product of its two principal curvature radii $R_1(\mathbf{k})$ and $R_2(\mathbf{k})$:

$$j(\mathbf{k}) \propto \frac{1}{G(\mathbf{k})} = R_1(\mathbf{k}) R_2(\mathbf{k}). \tag{2.2}$$

G is the Gaussian curvature at the location k on the Fermi surface in three-dimensional space. First experiments in the semimetal bismuth have shown enhanced carrier transport within three planes due to a huge but not infinite radius of curvature ($G \neq 0$) of the corresponding Fermi surface pockets.[1] For a location on the Fermi surface with at least one infinite radius of curvature ($G=0$), the electronic flux in real space in the corresponding group velocity direction becomes singular due to Eq. (2.2). The occurrence of such singularities or ''*caustics*'' is called *electron focusing* (EF),[1] in analogy to phonon focusing,[4] the related phenomenon of highly anisotropic phonon transport. Electron focusing has also been observed in the noble metal silver and in the transition metal tungsten.[2] These first experiments provided the motivation for a systematic study on the latter material for different crystal orientations and different geometries of the magnetic field.

In Fig. 1(b) the cross section of the octahedral hole Fermi surface of tungsten and the resulting current flux in real space are shown. Fig. 1(b)(I) corresponds to the central [110] cross section of the hole octahedron Fermi surface of tungsten. R becomes infinite, when the ''Fermi line'' changes curvature from convex to concave. This is equivalent to a change of the sign of the radius of curvature. The idealized ''Fermi line'' of tungsten in Fig. 1(a)(I), a square, produces two sharp focusing peaks, where the surface normals hit the detection plane [Fig. 1(a)(III)]. Due to the rounded corners and slightly inwards bent edges of the real ''Fermi line'' of tungsten there exist two locations with zero curvature on each side [▲ in Fig. 1(b)(I)], thus the peak of Fig. 1(a)(III) splits into two peaks [Fig. 1(b)(III)].

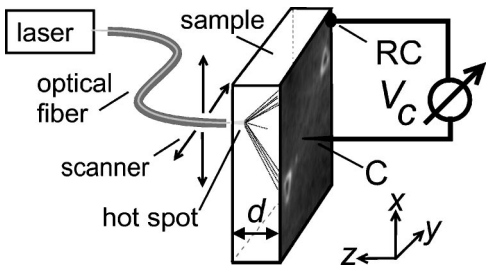

FIG. 2. Scheme of the experimental setup. A laser beam is coupled into an optical fiber, the end of which is brought close to the sample surface. An area of ($\approx 20\ \mu$m)^2 is illuminated, and carriers are excited thermoelectrically. To detect an EF pattern the fiber is scanned over the surface and the voltage V_C between the collector point contact C and a reference contact RC on the sample edge is detected as a function of the fiber position.

III. SETUP

Figure 2 shows a scheme of the setup. An argon-ion laser beam is chopped with frequency $f \approx 100$ Hz, and coupled into an optical fiber, the end of which is brought $\approx 20\ \mu$m close to the sample surface. An area of ($\approx 20\ \mu$m)^2 is illuminated with a power of ≈ 25 mW (hot spot). All experiments are performed with the sample immersed in liquid ^{4}He at $T=1.5$ K. The temperature difference between the cold crystal and the hot spot generates a thermal gradient and thus a thermoelectrical current. To detect an EF pattern, the fiber is scanned over the surface by a cryogenic scanner.[5] The voltage V_C between the collector point contact C and a reference contact RC on the sample edge is detected as a function of the fiber position. This is equivalent to a fixed hot spot and a scanning collector contact, if the investigated crystal is homogeneous (apart from spatial inversion). Because V_C is in the range of nV, phase-sensitive detection is used.

The samples were cut by spark erosion from single crystals to slabs of $d \approx 2$ mm thickness. The sample thickness was reduced to $\approx$ 0.16–0.37 mm by chemical etching[6] to expose the undisturbed bulk of the crystal (assumed to have an almost perfect lattice) and to reduce the thickness d of the sample to the dimensions of the expected mean free path. Samples with a surface perpendicular to the [110], [100], and [111] directions have been prepared. The (100) sample was cut slightly wedge shaped, with $d \approx$ 0.15, . . . ,0.3 mm for a diameter of ~ 10 mm in order to be able to investigate different sample thicknesses.

The mean free path l^* depends on the crystal quality, and varies strongly within the sample due to local distortions and impurities, but l^* can be estimated from the quality of the electron focusing patterns and is in the range of 0.4-0.5mm (see Secs. V B and V C). The residual resistance ratio (RRR) of the used samples was measured to $(15–20)\times 10^3$.

IV. FERMI SURFACE AND BAND STRUCTURE

Tungsten is a typical transition metal. The electronic properties are mainly dominated by the gradually filled in d

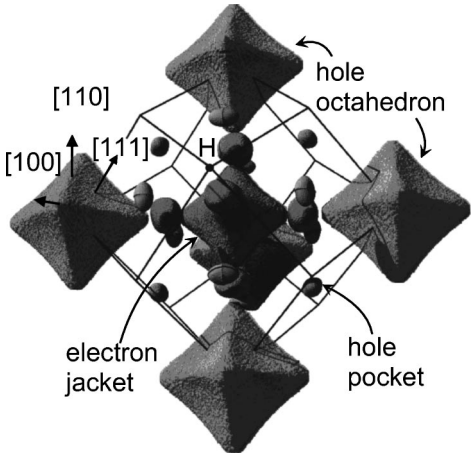

FIG. 3. Fermi surface of tungsten calculated with the band strucure given in Ref. 8. The hole octahedron at the *H* point oriented toward the observer is not shown in order to expose the ''jack'' structure in the center of the Brillouin zone.

band. Calculated band structures indicate that the *d* band lies high up in the conduction band and extends through the Fermi energy. The narrow *d*-band levels give rise to striking magnetic properties, and lead to low cyclotron frequencies.[7] The Fermi surface calculated with the band structure given by Ref. 8 is presented in Fig. 3. The six octahedron-shaped pockets at the zone corners (*H* point) and the 12 smaller pockets in the centers of the rhomboid Brillouin-zone faces contain holes. The latter are equivalent in pairs (from opposite faces). The structure in the center is an electron surface, called the ''jack.''[9] Tungsten is a compensated metal with an even number of electrons. Thus the volume of a large hole pocket plus six times the volume of a small hole pocket is equal to the volume of the electron pocket at the center of the Brillouin zone. It can be expected that the complicated Fermi-surface structures should produce quite complex electron-focusing patterns for both holes *and* electrons.

V. EXPERIMENTAL RESULTS AT $B=0$

Figures 4(a)–4(f) show electron-focusing patterns recorded on the [111], [110], and [100] surfaces of tungsten. The signal intensity is shown in gray scales as a function of the fiber position, such that the hole signal appears bright and the electron signal dark. No manipulation has been performed on the data. The electron focusing patterns (a)–(c) of Fig. 4 are shown in approximately the same image frame of $(0.6\ \text{mm})^2$. The EF patterns (d), (e), and (f) of Fig. 4 show close-ups on the triangular caustics of (a), (b), and (c), respectively.

The main contribution to the electron-focusing pattern stems from holes of the octahedron at the *H* point of the Fermi surface (see Figs. 3 and 5). Two different sets of states with zero Gaussian curvature exist for holes:

(1) States on the lines enclosing the concave regions on the triangular faces of the Fermi surface produce bright triangular caustics. Three bright spots at the edges of this triangle appear under an angle of $\approx 5°$ with respect to the $\langle 111\rangle$ directions (the [111] direction is indicated by ▲ in Fig. 4).

(2) States around the convex corners of the octahedron generate a series of faint lines connecting the triangles.

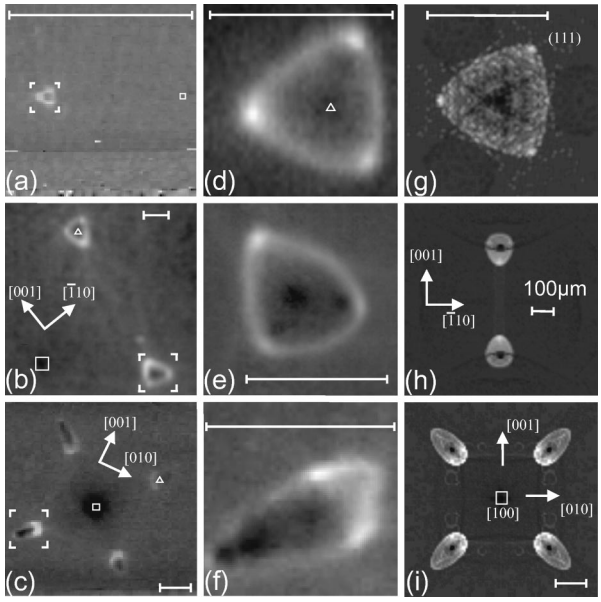

FIG. 4. Electron-focusing patterns of tungsten. The left two columns show experimental patterns obtained on surfaces of different crystallographic orientation, and the right column shows the corresponding simulated patterns using the band structure model from Ref. 8. The voltage V_C is presented in grey scale as function of the fiber position, such that the hole signal appears bright and the electron signal dark. (a) (111) surface, $0\ \text{nV} \leqslant V_C \leqslant 1.1\ \text{nV}$ from black to white, the image frame is $(0.6\ \text{mm})^2$ and the thickness of the crystal $d \approx 0.33$ mm. (b) (110) surface ($0\ \text{nV} \leqslant V_C \leqslant 1.8\ \text{nV}$), $(0.6\ \text{mm})^2$, and $d \approx 0.37$ mm. (c) (100) surface ($0\ \text{nV} \leqslant V_C \leqslant 0.61\ \text{nV}$), $(0.6\ \text{mm})^2$, and $d \approx 0.16$ mm. ■ and ▲ indicate the points where the [100] and the [111] directions cross the surface. The horizontal bars represent 100 μm. (d)–(f) Close-up of the pattern outlined by the white edges in (a)–(c). (g) Theoretical caustic on the (111) surface computed for holes and electrons, 10^4 trajectories have been traced for this image, and the frame is $0.7d$. (h) (110) surface, 10^5carriers, and the frame width is $2.5d$. (i) (100) surface, 10^5 trajectories, and the frame width is $4d$. The white horizontal bar represents 100 μm in the experimental images and the corresponding length scale in the simulated images.

Two different locations on the jack surface produce the electron caustics:

(1) Several dark spots are visible inside the bright triangles. The inner structure of the electronic jack resembles the hole octahedron, and presumably produces dark spots similar to the hole caustics but with inverted polarity.

(2) Spheres flattened in the $\langle 100\rangle$ directions and ''plugged'' onto the electron octahedron may be responsible for the dark structures appearing in the $\langle 100\rangle$ directions.

Depending on the orientation of the sample, one (for the [111] surface), two (for the [110] surface) or four (for the [100] surface) bright triangular caustics appear, which will now be described in greater detail.

A. (111) surface

Since the [111] pattern [Figs. 4(a) and 4(d)] represents a projection of all $\mathbf{v}_{gr}$ perpendicular to one octahedron face, the triangle is of threefold symmetry and equilateral. A dark spot in the center can be figured out [▲ in Fig. 4(d)]. Unfortunately the frame of the detected pattern is only

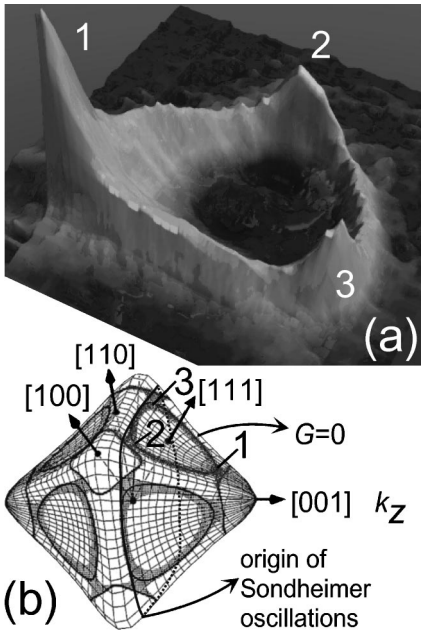

FIG. 5. (a) The electron focusing pattern for a [110]-oriented crystal in perspective representation [Fig. 4(d)]. The peaks are labeled from 1 to 3 for reference in the text (see text). (b) Hole octahedron Fermi surface of tungsten. States with Gaussian curvature $|G| \leqslant 10^{-21}$ m^2 are outlined. The cross section producing Sondheimer oscillations ($\partial^2 S_{k_z}/\partial k_z^2 = 0$) is indicated (see Sec. VI B).

$(100\ \mu\text{m})^2$, and as such it is quite small with respect to the resolution of the experiment given by the size of the ''hot spot'' $(20\ \mu\text{m})^2$. This is why smaller structures cannot be resolved in more detail.

B. (110) surface

Two bright triangular caustics and the faint lines connecting the triangles are clearly visible in the electron-focusing patterns detected in the [110] direction. The close-up of this pattern shown in Fig. 4(e) again reveals the three bright spots at the edges of the triangles. At least three dark spots are visible inside the triangle, and a fourth one can be guessed for symmetry reasons. Another dark structure can be seen where the [100] [■ in Fig. 4(b)] and [010] direction hit the surface [upper left and lower right parts of Fig. 4(b)]. Figure 5(a) shows a perspective representation of Fig. 4(e). It can be seen that the height of the peak number 1 in Fig. 5 is of approximately twice the height of the two outer peaks (2 and 3) for two (geometrical) reasons:

First, the carriers producing the inner peak have shorter trajectories t ($t = 0.43$ mm) with respect to the peaks 2 and 3 ($t = 0.48$ mm). So their scattering probability during their travel from the hot spot to the detection plane is lower than for these forming the two outer peaks.

Second, the signal is proportional to the current density component (i.e., the group velocity vector component) normal to the surface. This normal component is 13% greater for peak 1 carriers than for those producing peaks 2 and 3. Since the total intensity loss is not only 13%, but four times more ($\approx 50\%$), due to enhanced scattering for $t > 0.43$ mm, the mean free path l^* of holes can be estimated to be in the range of 0.43–0.48 mm.

C. (100) surface

The focusing pattern on the (100) surface shows four bright triangular caustics corresponding to the four faces of the hole octahedron. They appear where the $\langle 111 \rangle$ directions hit the surface. Since they enclose an angle of $\sim 55°$ with the [100] direction, the triangles are extremely stretched and deformed. Figure 4(f) shows a close-up of the pattern in Fig. 4(c). Dark structures from the electron octahedron are visible in the outer (left) part of the pattern. The four hole caustics are slightly different in size and in sharpness. This can first be explained by the wedge-shaped form of the sample. The sharpness is then reduced due to longer trajectories in the thicker part of the sample. Second, increased scattering due to partly lower crystal quality and irregularities of the mechanical scanning device cannot be excluded. The dark spot in the center due to electrons is clearly visible. Corresponding structures caused by electrons where the [100] direction hits the sample surface can be seen in Fig. 4(c), and should also be visible in Fig. 4(a), where they might not have been resolved for several possible reasons.

First, the [111] oriented crystal is apparently of lower quality than the other crystals.

Second, the electron signal in tungsten is generally less intensive than the hole signal. A similar behavior has been observed for holes in bismuth.[1]

Third, in the [111]-oriented sample of 330-μm thickness, electron trajectories are 3.5 times longer than in the [100]-oriented sample of 160-μm thickness, and thus are more exposed to scattering. In addition, these electrons hit the (111) surface under an angle of $\sim 35°$ (90° for the [100] sample). This would reduce the signal by the factor sin 35°.

Since the electron contribution is visible in the [100] and [110] samples and not in the [111] sample, the electron mean free path can be estimated to about 0.5 mm.

VI. EXPERIMENTAL RESULTS IN FINITE MAGNETIC FIELDS

A. Transverse magnetic field

The focusing patterns of one triangular bright caustic on the (110) surface were recorded for different transverse magnetic fields **B** applied in the [001] direction. Some results are shown in Figs. 6(a)–6(e). With increasing B_t, peak 2 fades out in favor of peak 3 and of the dark spot in its vicinity ($B = 6.4$ mT). At $B = 7.3$ mT the triangular bright pattern is deformed, peak 3 now surpasses peak 1 in intensity. Finally peak 2 and even peak 1 disappear together with the bright lines connecting them. The dark structure becomes more and more intense and approaches the bright peak which has its highest value at $B = 10.5$ mT. In fields higher than 10.5 mT, peak 3 also starts to decrease and the dark structure dominates the pattern. This series of focusing patterns nicely illustrates the gradual changes introduced by the application of **B**. That the pattern deforms, shrinks, and finally disappears is consistent with the model of ballistic carrier propagation: The carrier trajectories, which are straight lines for $B = 0$, are bent by the magnetic field. The real-space orbit represents the k space cross-section of the Fermi surface perpendicular to **B** through the corresponding k_F and scaled by the factor $\hbar/eB$ (see Sec. VII B). Thus the diameters of the orbits form-

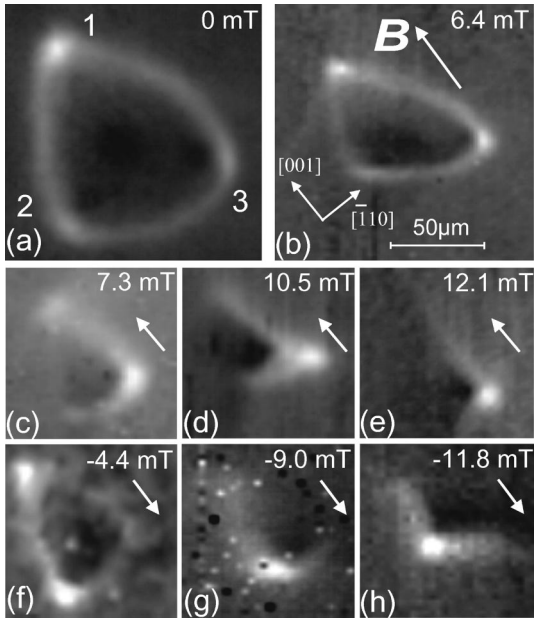

FIG. 6. The electron focusing pattern of Fig. 4(e) for different transverse magnetic fields $\mathbf{B}_t$. $\mathbf{B}_t$ is applied as indicated in the [001] direction for (a)–(e) and in the $[00\bar{1}]$ direction for (f)–(h). The scale for all figures is the same, and is indicated in (b). The peaks are labeled 1, 2, and 3 for reference in the text.

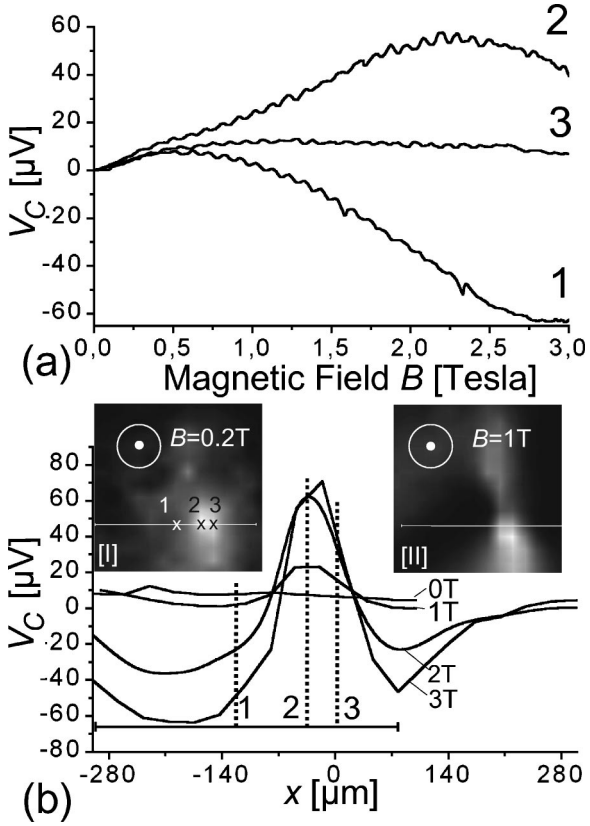

FIG. 7. (a) Sondheimer oscillations at positions 1, 2, and 3 indicated by the crosses in (b)(I). (b) V_C is shown as a function of the position on a line scan for several values of a magnetic field **B** applied perpendicular to the image plane. The crystal is the same used already for Figs. 4(c) and 4(f). The orientation of the line scan is shown as a white bar in the two insets (I) and (II) which show the spatial behavior of V_C for the two fixed B values noted in the insets. The image frame width is 400 μm.

ing the caustics ($G=0$) shrink with increasing B, and finally become smaller than the sample thickness d.

Holes and electrons as well as states with different energy levels are differently influenced by B. For inverse magnetic fields the electron-focusing patterns behave in the same way, but mirrored such that the behaviors of peaks 2 and 3 are exchanged. This is illustrated in Figs. 6(f)–6(h). Unfortunately these patterns are very noisy. This maybe due to mechanical vibrations of our scanning unit.

B. Longitudinal magnetic field $\mathbf{B}_l$

The (100) surface was investigated with **B** perpendicular to the sample surface. Now the carriers move on generalized helical trajectories that wind around **B**.

All ballistic trajectories with the same k_z component, and the same energy value E_F cross each other in one common point after an integer number n of revolutions. They all come from the same Fermi-surface cross section S_{k_z} perpendicular to the magnetic field. For certain magnetic fields,

$$B_{foc}(k_z^{foc}) = \frac{n\hbar}{de}\left(\frac{\partial S_{k_z}}{\partial k_z}\right)_{E=E_F}, \tag{6.1}$$

the crossing point lies on the opposite sample surface and so-called longitudinal electron focusing occurs.[10] Here d is the sample thickness, and e is the electron charge. As Eq. (6.1) is valid for each S_{k_z} along k_z, nearly all longitudinal focusing features interfere destructively for a given B. Only contributions from so-called extreme cross sections survive. These are either so-called elliptical limiting-points (points where k_z becomes maximal), or cross sections where the value $\partial^2 S_{k_z}/\partial k_z^2$ vanishes. From these locations on the Fermi surface so-called Sondheimer oscillations periodic in B with the oscillation period B_{foc} can be detected.[11,12] This has been proved by radio-frequency size effect, magnetoresistance, and magnetomorphic measurements in tungsten single crystals.[13,14] From B_{foc} the value $\partial S_{k_z}/\partial k_z$ can be obtained using Eq. (6.1). The corresponding Fermi-vector component k_z^{foc} can be deduced from the Fermi-surface data.

In tungsten the electron signal seems to be less intensive than the hole signal (see Sec. V) and the elliptical limiting points of the hole pockets and of the hole octahedron would give only low-amplitude signals. This is why one can expect Sondheimer oscillations only from the cross-section of the hole octahedron fulfilling the condition $\partial^2 S_{k_z}/\partial k_z^2 = 0$.

V_C is shown as a function of B at three different positions on the sample surface in Fig. 7(a). Oscillations strictly periodic in B up to 3 T are clearly visible for all three positions. We interpret them as Sondheimer oscillations. According to Ref. 13 the oscillations in tungsten can be observed everywhere on the sample because of scattering and reflection of the carriers at the sample surfaces.

The oscillation period is $B_{foc}=104$ mT for $d \approx 0.19$ mm. The value $\partial S_{k_z}/\partial k_z \approx 3\times 10^{10}$ m^{-1} resulting from Eq. (6.1) is in good agreement with other measurements of Sondheimer oscillations in tungsten single

crystals.[13,14] With $E(\mathbf{k})$ from Ref. 8, we found $\partial^2 S_{k_z}/\partial k_z^2 = 0$ for the focusing wave vector $k_z^{foc} = 0.1 \times 10^{10}$ m^{-1} and $\partial S_{k_z}/\partial k_z = 3.3 \times 10^{10}$ m^{-1}. This is in good agreement with the theoretical value given by Soule using his own model.[14] Applying the Fermi surface data given by Girvan,[9] however, he arrived at $\partial S_{k_z}/\partial k_z = 3.0 \times 10^{10}$ m^{-1} for the focusing wave vector $k_z^{foc} = 0.23 \times 10^{10}$ m^{-1}. The values 0.1×10^{10} m$^{-1} \leqslant k_z^{foc} \leqslant 0.23 \times 10^{10}$ m^{-1} correspond to states near the equatorial bulge around the H point of the Brillouin zone and are indicated in Fig. 5(b).

The occurrence of the Sondheimer effect proves the existence of a noticeable part of ballistic transport for fields up to 3 T. This is in contrast to the case of bismuth, where they die out already below 15 mT (Ref. 15). However, one may conclude from the data shown in Fig. 7(a) that the ballistic component of the total current is in the range of several percent only. This maybe too weak to produce some pronounced features in the spatially resolved measurements as it has been observed in bismuth.

Along the line indicated in the insets (I) and (II) of Fig. 7(b), the signal intensity V_C was detected as a function of the x coordinate for different magnetic fields. It can be seen that the signal intensity of the central peak increases with increasing magnetic field. An intense dark structures develop in the pattern. In general the features in V_C are amplified by the application of B. This behavior is frequently observed in electron focusing experiments in high fields.

The ballistic contribution to the signal is confined to a tube with diameter $4r_c^*$, where r_c^* is the cyclotron radius of the largest trajectories of holes on the octahedral Fermi surface. The trajectory envelope shrinks in diameter proportional to B^{-1} with increasing $\mathbf{B}$. At $B = 0.2$ T [corresponding to the situation in Fig. 7(b)(I)] one obtains $4r_c^* = 120\mu$. This corresponds to the full width at half maximum of the Gaussian-like peak visible in the center of Fig. 7(b). But at $B = 1$ T [corresponding to the situation in Fig. 7(b), (II)] all ballistic carriers should be focused on a small area with diameter $4r_c^* = 24$ μm. Since this is not the case one can conclude that the electron-focusing pattern at higher fields is dominated by nonballistic processes.

According to Ref. 13 any diffusive background signal should be proportional to B^2 for one kind of carriers. This is only the case for $B \leqslant 0.2$ T. For higher fields the background even becomes negative at certain positions. In addition the symmetry of the patterns is not fourfold, but rather twofold, and the patterns are not centered in the image.

We suppose that the background in our measurements is of mainly diffusive nature. The signal is probably composed of electron and hole contributions. Different trajectories and different mean free paths depending on the magnetic field may then lead to a changing dominance of one type of carrier with $\mathbf{B}$. Thus the condition $V_C \propto B^2$ is not fulfilled for the total signal. In addition boundary effects seems to become more important when the signal is amplified by the magnetic field. Why this is the case is not clear. Boundary effects can be the influence of the geometry of the reference contact on the sample, the nonideal shape of the sample itself, and the positioning of the measurement frame, which is usually situated near one of the sample edges. Thus an appropriate theoretical description of the origin of the background signal in Fig. 7(b) for $B_l \geqslant 0.2$ T may be quite complex.

VII. SIMULATIONS OF THE RESULTS

A. $B = 0$

The band structure $E(\mathbf{k})$ of tungsten is available from a Slater-Koster interpolation scheme based on the lowest combination of atomic orbitals method.[8] The EF patterns are computed assuming $V_C \sim j_n$, where j_n is the current density component normal to the surface. $\mathbf{k}_F$ and $\mathbf{v}_{gr}$ are determined for up to 10^7 random $\mathbf{k}$ directions. All the calculations are done assuming an infinite mean free path and an infinitesimal size of the electron source. Only electrons with $E = E_F$ are taken into account.

For a random direction in $\mathbf{k}$ space the Fermi vector $\mathbf{k}_F$ is calculated from $E(\mathbf{k}_F) = E_F$ by iteration. The group velocity $\mathbf{v}_{gr}$ is then determined by calculating $\nabla_k E(k_F) \approx \Delta E(k_F)/\Delta k$ for a given sufficiently small Δk. The resulting trajectory emerging from a pointlike source intersects with the imaging plane in a distance d. The contribution of all trajectories are summed up in the image plane, each weighted with the group velocity component normal to the surface and the factor $\mathbf{k}_F^2(\mathbf{k}_F/|\mathbf{k}_F| \cdot \mathbf{v}_{gr}/|\mathbf{v}_{gr}|)^{-1}$ in order to ensure homogenous sampling in $\mathbf{k}$ space.

In Figs. 4(g)–4(i) the calculated focusing patterns for the three investigated crystals are shown for $B = 0$. As the band structure given by Ref. 8 describes the triangular structures better if the Fermi energy is lowered by 0.23 eV, the value $E_F = 10.88$ eV is used for all calculations. With this small parameter change the details of the calculated patterns are better reproduced, but the size of the triangular structures is too large with respect to their distance. The general appearance of the theoretical caustics agrees with the experimental one, i.e., the triangular hole structures with three bright spots on its boundary and the locations of the dark electron caustics. However, the agreement of details is quite bad. Thus, even if this band-structure model describes de Haas–van Alphen data very well they do not reproduce Fermi-surface regions where $G = 0$ with sufficient precisision. This demonstrates the high sensitivity of the electron focusing patterns for details of the Fermi-surface geometry. This sensitivity is still more important in the presence of a magnetic field.

B. Transverse magnetic field $\mathbf{B_t}$

Since the deformation of the patterns by a transverse magnetic field $\mathbf{B}$ cannot be deduced with straightforward arguments we calculated the hole trajectories for $0 \leqslant B_t \leqslant 15$ mT. In a magnetic field the equation of motion of an electron is

$$\hbar \frac{d\mathbf{k}}{dt} = -e[\mathbf{v}_{gr}(\mathbf{k}) \times \mathbf{B}]. \tag{7.1}$$

$\mathbf{v}_{gr}(\mathbf{k})$ is always perpendicular to $E(\mathbf{k}) = \text{const}$, and the energy E as well as k_z are constants of motion. Therefore the carrier will move on the Fermi surface on an orbit around $\mathbf{B}$.

Performing an integration on Eq. (7.1) yields

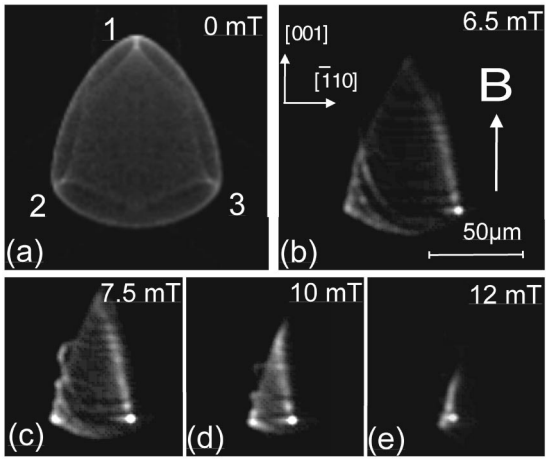

FIG. 8. Calculated electron focusing patterns from a [110]-oriented sample at different transverse magnetic fields corresponding to Figs. 6(a)–6(e); only holes are taken into account. The field magnitude is indicated in the figures. Because of the granular appearance of the original theoretical images, they have been smoothed by a Gaussian with 5% of the total frame width. The peaks are labeled 1, 2, and 3 for reference in the text. The scale for all figures is the same and is indicated in (b), and the sample thickness is $d=350\ \mu$m.

$$\mathbf{r}(t+dt)-\mathbf{r}(t)=d\mathbf{r}=-\hbar/(eB)[\mathbf{k}(t+dt)-\mathbf{k}(t)] \tag{7.2}$$

for $\mathbf{B}\perp\mathbf{v}_{gr}$. To calculate the trajectory in a magnetic field for a given $\mathbf{k}_F$ chosen on a regular array, the group-velocity vector $\mathbf{v}_{gr}(\mathbf{k}_F)$ can be obtained from Eq. (2.1). $d\mathbf{k}$ is calculated from Eq. (7.1) with $|d\mathbf{k}|=\Delta k$. The value Δk is a constant parameter of the calculation and is small with respect to all other occurring $\mathbf{k}$ values. Keeping $|d\mathbf{k}|=$const ensures a homogeneous sampling on the cross-section orbit. With $d\mathbf{k}\approx\mathbf{k}_F(t+dt)-\mathbf{k}_F(t)$ the corresponding time element dt and, using Eq. (7.2), the trajectory segment $d\mathbf{r}$ can be obtained. The following trajectory segment $d\mathbf{r}$ is then calculated for the value $\mathbf{k}_F=\mathbf{k}_F(t+dt)$ with the same scheme. This is repeated until the cross-section orbit on the Fermi surface is completed. The real space trajectory is then composed of the $d\mathbf{r}$ elements. The carriers move in $\mathbf{k}$ space on cross sections perpendicular to $\mathbf{B}$. This is why the calculation of one orbit yields any possible orbit. Only the position of the starting point of the orbit depends on the initial $\mathbf{k}$ state. For different magnetic fields the trajectories just scale as $1/B$.

In Figs. 8(a)–8(e) the simulations of the detected patterns of Figs. 6(a)–6(e) are shown. Only carriers of one kind (i.e., holes from the octahedron at H) at E_F were taken into account. The shrinking of the whole pattern and the inversion of the curvature of the bright lines with increasing $\mathbf{B}$ is reproduced by the calculations. However, the deformations of the structures at lower fields as well as the field dependence of the caustic intensities do not correspond well to the experiment.

As described above the determination of $\mathbf{v}_{gr}$ uses an iterative search for $\mathbf{k}_F$. Solving Eq. (7.2) with sufficient accuracy requires several hundred $\mathbf{k}_F$ values to be computed. Either powerful computers or extensive processing times are needed (for the simulations presented here we used a CRAY T3E). So the number of computed trajectories is restricted to 10^4 here and the theoretical images have a granular and noisy appearance. In addition they are composed of lines, this is a computational artifact stemming from the regular sampling of the $\mathbf{k}_F$ states which was used here instead of a random sampling of the Fermi surface.

This is another example, which shows how sensitive electron focusing reacts on small details of the Fermi-surface geometry. The band-structure data from Ref. 8 are apparently not realistic enough, though they fit very well the de Haas–van Alphen data. A better agreement between simulation and experiment could perhaps be attained by using a better model for $E(\mathbf{k})$, by introducing a thermal excitation spectrum as proposed in Ref. 2 or by including carriers from the other pockets of the Fermi surface in the calculations (the vanishing features in the caustics at higher fields could very well be due to a cancellation of signals from carriers of opposite charge or opposing currents of carriers of one kind of charge). But handy data, which describe details of the Fermi surface with sufficiently high accuracy, are not easily available, and these algorithms may not be easy to implement in our computational procedure. In addition more computing power would be necessary, especially if a thermal excitation spectrum is to be taken into account. We considered this task to be beyond our reach. It may rest as a challenge for future theoretical work.

VIII. CONCLUSIONS

We have presented experiments revealing the mainly ballistic transport of carriers excited thermoelectrically by illumination in tungsten. Electron-focusing caustics in $V_C(\mathbf{r})$ have been observed in three orientations. To our knowledge, this is the first systematic study of electron focusing in three different crystal orientations. The complex Fermi surface of tungsten produces electron-focusing patterns mainly for holes, but focusing structures for electrons have also been found. These results are supported by simulation and by the investigation of different orientations, principally by the (100) surface, where the most important electron structures have been detected. The influence of longitudinal and transverse magnetic fields was studied in two different crystal orientations. In a transverse magnetic field the bending of the trajectories by the field and the resulting distortion of the triangular focusing pattern have been observed. In a longitudinal field geometry the focusing of the trajectories on a peak can be observed for $B_l\leqslant 0.2$ T. Other bright and dark structures for high magnetic fields cannot be interpreted exactly. Oscillations strictly periodic in B have been observed for $V_C(B)$ up to 3 T. The background signal is not proportional to B^2, and can be positive or negative depending on the position. The oscillations are due to the Sondheimer effect, and demonstrate partly ballistic transport up to 3 T. The period is in agreement with other experimental and theoretical data. The corresponding cross section on the hole octahedron can be identified by the calculation of an extreme point of $\partial S_{k_z}/\partial k_z$.

By solving the semiclassical Eqs. (2.1) and (7.1), the ballistic carrier transport can be simulated without and in the presence of a magnetic field. The results depend on the quality of the band-structure used. The $E(\mathbf{k})$ used here presents a quite recent and handy model. It provides a quite good agree-

ment between calculated focusing patterns and experimental data for $B=0$.

The simulations of the magnetic-field dependence of the focusing patterns reproduce the main features, but it is not in very good quantitative agreement with the experimental measurement. A lot of computational power is necessary for these simulations, and more actual and yet handy data for $E(\mathbf{k})$ have not been found.

Since the technique presented here is very sensitive to very small changes in Fermi-surface structures, the imaging of details of the Fermi surface is possible. This gives the possibility to check band-structure models as presented here for the data from Ref. 8. The results presented here may be an incentive and touchstone for band-structure theoreticians.

ACKNOWLEDGMENTS

We wish to thank D. A. Papaconstantopoulos for generously making his programs available to us and the Centre d'Etudes Nucleaire de Grenoble (CENG) for the numerous hours of calculation time on its CRAY T3E. We are sincerely grateful to V.S. Tsoi and V.L. Gurevich for their attention to this work. We acknowledge the financial support for this work from the European Union and the Deutscher Akademischer Austausch-Dienst.

[1] J. Heil, M. Primke, and K. U. Würz, Phys. Rev. Lett. **74**, 146 (1995).
[2] J. Heil, M. Primke, A. Böhm, J. Major, P. Keppler, and P. Wyder, Phys. Rev. B **54**, 2280 (1996).
[3] A. M. Kosevich, Fiz. Nizk. Temp. **11**, 611 (1985) [Sov. J. Low Temp. Phys. **11**, 611 (1985)].
[4] J. P. Wolfe, *Imaging Phonons* (Cambridge University Press, Cambridge, 1998).
[5] J. Heil, A. Böhm, M. Primke, and P. Wyder, Rev. Sci. Instrum. **67** (1), 307 (1996).
[6] 2–3 parts HF (40%)+ 1 part HNO_3 (65%), room temperature.
[7] W. Ashcroft and N. D. Mermin, *Solid State Physics* (Sanders College Press, 1976), p. 306.
[8] D. A. Papaconstantopoulos, *Handbook of the Band Structure of Elemental Solids* (Plenum Press, New York, 1986).
[9] R. F. Girvan, A. V. Gold, and R. A. Phillips, J. Phys. Chem. Solids **29**, 1485 (1968).
[10] Yu. V. Sharvin and L. M. Fisher, Zh. Éksp. Theor. Fiz. Pis'ma Red. **1**, 54 (1965) [JETP Lett. **1**, 152 (1965).
[11] E. H. Sondheimer, Phys. Rev. **80**, 401 (1950).
[12] V. L. Gurevich, Zh. Éksp. Teor. Fiz. **35**, 668 (1958) [Sov. Phys. JETP **8**, 464 (1959)].
[13] A. M. Grishin P. P. Lutsishin, Yu. S. Ostroukov, and O. A. Panchenko, Zh. Éksp. Teor. Fiz. **76**, 1325 (1979) [Sov. Phys. JETP **49**, 673 (1979)].
[14] D. E. Soule and J. C. Abele, Phys. Rev. Lett. **23**, 1287 (1979).
[15] M. Primke, J. Heil, A. Böhm, A. Gröger, and P. Wyder, Phys. Rev. Lett. **79**, 4882 (1997).